Interleaved Model Predictive Control for Three-Level Neutral-Point-Clamped Dual Three-Phase PMSM Drives With Low Switching Frequencies

Minrui Gu , *Student Member, IEEE*, Zheng Wang , *Senior Member, IEEE*, Kailiang Yu, *Student Member, IEEE*, Xueqing Wang , *Member, IEEE*, and Ming Cheng , *Fellow, IEEE*

Abstract—In this article, the control strategy is studied for the neutral-point-clamped three-level inverter-fed dual three-phase permanent-magnet synchronous motor (PMSM) drive with low switching frequencies. An interleaved finite-control-set model predictive control (MPC) scheme is proposed, where a two-layer MPC is designed to solve the multiobjective optimization problem. The two sets of windings in PMSM are sampled and controlled in an interleaved way so that the control delay and the prediction horizon of the drive system are reduced by half. Moreover, the proposed interleaved control scheme increases the equivalent sampling and control frequency from the perspective of the whole drive system, and thus provides better steady-state performance and dynamic performance. With the switching states of one inverter remaining unchanged, the cross traversal of vector candidate sets between two sets of windings is avoided, and the computational burden can be reduced effectively. Experimental results are given to verify the validity and effectiveness of the proposed interleaved control scheme.

Index Terms—Dual three-phase permanent-magnet synchronous motor (PMSM) drive, low switching frequency, model predictive control (MPC), multiphase interleaved control, neutral-point-clamped three-level (NPC-3L) inverter.

I. INTRODUCTION

RECENTLY, with the increasing demands for medium-voltage (MV) high-power electric drive systems, multilevel converters have drawn more attention in industrial applications. The main superiority of the multilevel converters can be summarized as lower voltage pressure for devices, higher quality of output voltages, higher efficiency, higher reliability, and less electromagnetic interference [1], [2]. Among various multilevel

topologies, the neutral-point-clamped three-level (NPC-3L) inverters have been widely applied due to the merits of their simple structures. At the same time, the multiphase machines have been popular in MV high-power applications. The main advantages offered by multiphase drives include more degrees of control freedom, lower torque ripple, lower current stress, lower dc-link current pulsation, and high fault-tolerant capability [3]–[6]. By combining the techniques of multilevel converters and multiphase machines, the multiphase multilevel drives become promising solutions for MV high-power ac drives [7], [8].

In MV high-power applications, the switching frequencies are usually limited to less than 1 kHz to ensure efficiency and satisfy the thermal constraints [9], [10]. However, the limited switching frequency is still the bottleneck for good control performance in high-power drives. Intensive studies have been given for high-power drives with low switching frequencies. The significant delay caused by the low sampling frequency reduces the control bandwidth and deteriorates the control performance. Therefore, the proportional–integral (PI) current controller has been specially designed to mitigate the impacts of the control delay in [11]. In recent years, the finite-control-set model predictive control (FCS-MPC) offers an attractive solution with the advantages of fast dynamic response and convenient implementation for multiobjective optimization [12]. In [13], the factors affecting the performance of FCS-MPC have been discussed and analyzed comprehensively, and guidelines are provided to improve the control performance. The high sampling frequency in FCS-MPC can naturally mitigate the impacts of the control delay, and the low switching frequency operation can also be achieved by adding the switching frequency into the cost function conveniently.

Generally, in FCS-MPC schemes, there exists a contradiction between the computational burden and the prediction horizon for high-power drives with limited switching frequencies. For lower computational complexity, the one-step prediction method is usually used in FCS-MPC [14]. However, the longer horizon can naturally ensure better control performance, whereas leading to the exponential increase of computational burden [15]. The trajectory extrapolation method is considered as a popular approach to solve this contradiction [16]. First, the best possible switching sequences are selected in the predefined switching horizon period. Second, the linear trajectory extrapolation is utilized to evaluate the steps for different voltage vectors to hit

the predefined error bounds. Based on the trajectory extrapolation method, a kind of model predictive direct torque control (DTC) is proposed in [17]. The main idea is to perform the MPC algorithm to find the best switching sequence for DTC instead of the look-up table method so that the switching frequency can be optimized during the selection of the next switching sequence. Another approach for reducing the computational burden is to narrow down the traversal range. In [18], the nearest three vector (NTV) principle is used to choose the voltage vectors for synthesizing the voltage reference. Similarly, the feasible control set is limited to the sector comprised of the nearest vectors, and the control algorithm is simplified effectively in [19].

However, previous research work on MPC with low switching frequency is mainly focused on three-phase drive systems. As mentioned above, the dual three-phase motor drives have more degrees of control freedom. In [20], a collaborative switching strategy is proposed, where the dc-link current ripple for the drive is mitigated by optimizing the switching sequences of the two three-phase inverters collaboratively. In this article, the additional freedom in instants for sampling and implementing control algorithm has been utilized fully for NPC-fed dual three-phase permanent-magnet synchronous motor (PMSM) drives. In the proposed interleaved MPC scheme, the sampling and the implementation of the control algorithm are conducted sequentially for the two sets of windings, so that the equivalent frequency of sampling and control for the whole drive is doubled. Additionally, the interleaved control scheme avoids the cross traversal of the voltage vectors in the two sets of three-phase windings. Thus, it can mitigate the high complexity in the MPC scheme for the dual three-phase PMSM drives effectively while achieving higher sampling frequency and better control performance. However, the proposed interleaved control scheme reduces the number of controllable variables from four to two. But there are still 4-D objective variables to be controlled in the dual three-phase PMSM drive. Therefore, there exists the problem that the dimension of control objectives exceeds the dimension of controllable variables, which can be regarded as one circumstance of the multiobjective optimization problem (MOOP).

A well-known solution is to convert the MOOP into a single-objective optimization problem with weighting factors. However, there exist more evident conflicts between the four control objectives, and the difficulty of tuning the weighting factors will be increased. Another method to handle the MOOP problem is to establish the multilayer cost function, also known as the sequential MPC (SMPC) proposed in [21]. In the first layer of evaluation, two vectors with the smallest values of the torque cost function are selected. In the second layer, the final vector is chosen with an independent flux cost function based on the two selected vectors in the previous step. In [22], the generalized SMPC control scheme is proposed and verified to be effective over the full-speed range without limitations on the execution order of the multilayer cost functions. Furthermore, the tolerance SMPC is proposed in [23] with the improvement in adaptability and flexibility compared with the conventional SMPC. Inspired by the SMPC schemes in [21]–[23], a two-layer interleaved MPC scheme is proposed in this article. Based on the vector space decomposition (VSD), the four objective variables of the dual
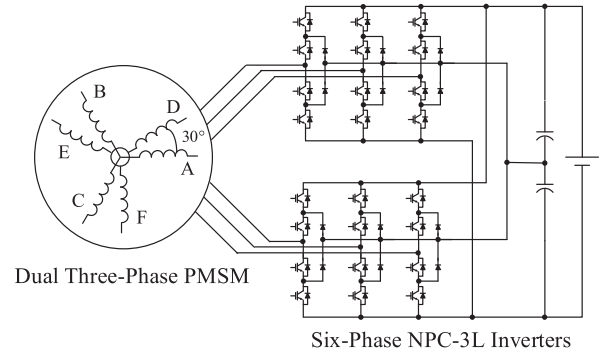

Fig. 1.   Configuration of the dual three-phase PMSM drive system.

three-phase PMSM drive are classified into two groups. The first group is comprised of torque-irrelevant variables, utilized for the first-layer evaluation. The second group is comprised of the torque-relevant variables, utilized for the second-layer evaluation. Different from the SMPC schemes in [21]–[23], the first layer is embedded in the deadbeat control to narrow the range of the vector candidates. The tracking error of the torque-irrelevant variables is not rigorous but naturally limited in a certain range, which is determined by the generation of the vector candidates in the first-layer evaluation. The superiority of the proposed two-layer MPC is that the purpose of narrowing the traversal range with deadbeat control and the purpose of controlling torque-irrelevant variables can be achieved simultaneously.

The organization of the rest of this article is listed as follows. The configuration and the discrete-time model of NPC-fed dual three-phase PMSM drives are described in Section II. Then, the synchronous MPC scheme of the dual three-phase PMSM with low switching frequencies is illustrated in detail in Section III. In Section IV, a two-layer interleaved MPC control scheme is proposed and described. The experimental verification is given to compare the performance between the proposed interleaved MPC control scheme and the synchronous MPC control scheme for the dual three-phase PMSM drive in Section V. Finally, Section VI concludes this article.

II. CONFIGURATION AND MODELING

Fig. 1 shows the configuration of the dual three-phase PMSM drive system. The dual three-phase PMSM is driven by two sets of three-phase NPC-3L inverters, whose dc links are connected in parallel.

A. Modeling of NPC-3L Inverter

Fig. 2 shows the equivalent circuit of a three-phase NPC-3L inverter. The positive current direction is specified in Fig. 2. Each leg of the NPC-3L inverter can generate three voltage levels, namely P, O, and N, which is equivalent to a single-pole three-throw switch.

The switch function of the NPC-3L inverter is defined as

$$S_x = \begin{cases} 1 \text{ output P level} \\ 0 \text{ output O level} \quad x \in \{a, b, c, d, e, f\} \\ -1 \text{ output N level.} \end{cases} \quad (1)$$
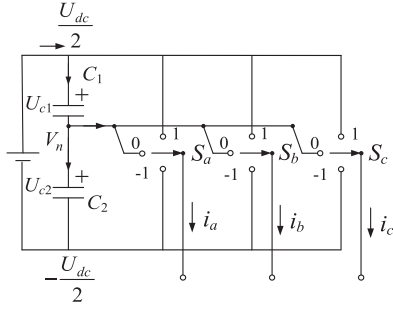
Fig. 2.   Equivalent circuit of a three-phase NPC-3L inverter.

The midpoint voltage, i.e., V_n in the dc link is calculated as

$$V_n = \frac{U_{c2} - U_{c1}}{2} \tag{2}$$

where U_{c1} and U_{c2} are the voltages of capacitors C_1 and C_2, respectively. According to the direction of current flows, the differential equation of V_n is obtained as

$$pV_n = \frac{-1}{2C} \sum_x (1 - |S_x|) i_x, x \in \{a, b, c, d, e, f\} \tag{3}$$

where C is the capacitance of dc-link capacitors C_1 and C_2, p is the differential operator, and i_x is the phase current.

B. Mathematical Model of Dual Three-Phase PMSM

The neutral points of two sets of windings in dual three-phase PMSM are isolated from each other. There is a 30° shifted angle between the dual three-phase windings. Under the dual dq-frames, the field-oriented control (FOC) is adopted to control the dual three-phase winding. The zero-sequence component of the three-phase PMSM is negligible due to the isolation between two sets of windings. It should be noted that there still exist cross-coupling effects between the two sets of three-phase windings. Therefore, the control of the dual three-phase motor is required to consider the mutual influence of the two three-phase windings, which is different from the control of two independent three-phase motors. The continuous-time form of the mathematical model in dual dq-frame is derived in [18], which is presented in the following equation:

$$\begin{cases} u_{d1} = R_s i_{d1} + L_d p i_{d1} + L_{dm} p i_{d2} - \omega L_q i_{q1} - \omega L_{qm} i_{q2} \\ u_{q1} = R_s i_{q1} + L_q p i_{q1} + L_{qm} p i_{q2} + \omega L_d i_{d1} + \omega \psi_f \\ \quad + \omega L_{dm} i_{d2} \\ u_{d2} = R_s i_{d2} + L_d p i_{d2} + L_{dm} p i_{d1} - \omega L_q i_{q2} - \omega L_{qm} i_{q1} \\ u_{q2} = R_s i_{q2} + L_q p i_{q2} + L_{qm} p i_{q1} + \omega L_d i_{d2} + \omega \psi_f \\ \quad + \omega L_{dm} i_{d1} \end{cases} \tag{4}$$

where L_d and L_q are the d-axis and the q-axis inductances, respectively, L_{dm} and L_{qm} are the d-axis and q-axis mutual inductance, respectively, R_s is the stator resistance, ψ_f is the magnitude of rotor magnetic flux produced by permanent magnets (PM), u_{d1} and u_{q1} are the d-axis and q-axis voltages of the first winding, respectively, u_{d2} and u_{q2} are the d-axis and q-axis voltages of the second winding, separately, i_{d1} and i_{q1} are the d-axis and q-axis currents of the first winding, respectively,

i_{d2} and i_{q2} are the d-axis and q-axis currents of the second winding, separately, and ω is the electrical speed of the rotor. This variable is considered almost unchanged during the period from instant kT_s to instant $(k+2)T_s$ due to the larger mechanical inertia compared to the electrical inertia [24].

By selecting i_{d1}, i_{q1}, i_{d2}, and i_{q2} as the state variables, the state equations can be derived from (4), which is presented in the following equation:

$$\dot{x} = Ax + Bu \tag{5}$$

where $x = [i_{d1} \; i_{q1} \; i_{d2} \; i_{q2}]^T$ is the state vector, and $u = [u_{d1} \; u_{q1} \; u_{d2} \; u_{q2} \; \omega\psi_f]^T$ is regarded as the input state vector. A and B are the system matrices, and the expressions are shown as follows:

$$A = \begin{bmatrix} A_{11} & A_{12} \\ A_{21} & A_{22} \end{bmatrix} \tag{6}$$

$$A_{11} = \begin{bmatrix} \frac{-L_d R_s}{L_d^2 - L_{dm}^2} & \frac{\omega L_d L_q - \omega L_{dm} L_{qm}}{L_d^2 - L_{dm}^2} \\ \frac{\omega L_{dm} L_{qm} - \omega L_d L_q}{L_q^2 - L_{qm}^2} & \frac{-L_q R_s}{L_q^2 - L_{qm}^2} \end{bmatrix} A_{22} = A_{11} \tag{7}$$

$$A_{12} = \begin{bmatrix} \frac{L_{dm} R_s}{L_d^2 - L_{dm}^2} & \frac{\omega L_d L_{qm} - \omega L_{dm} L_q}{L_d^2 - L_{dm}^2} \\ \frac{\omega L_d L_{qm} - \omega L_{dm} L_q}{L_q^2 - L_{qm}^2} & \frac{L_{qm} R_s}{L_q^2 - L_{qm}^2} \end{bmatrix} A_{21} = A_{12} \tag{8}$$

$$B = \begin{bmatrix} \frac{L_d}{L_d^2 - L_{dm}^2} & 0 & \frac{-L_{dm}}{L_d^2 - L_{dm}^2} & 0 & 0 \\ 0 & \frac{L_q}{L_q^2 - L_{qm}^2} & 0 & \frac{-L_{qm}}{L_q^2 - L_{qm}^2} & \frac{-1}{L_q + L_{qm}} \\ \frac{-L_{dm}}{L_d^2 - L_{dm}^2} & 0 & \frac{L_d}{L_d^2 - L_{dm}^2} & 0 & 0 \\ 0 & \frac{-L_{qm}}{L_q^2 - L_{qm}^2} & 0 & \frac{L_q}{L_q^2 - L_{qm}^2} & \frac{-1}{L_q + L_{qm}} \end{bmatrix}. \tag{9}$$

As described in Section I, the MPC method could offer a solution to improved operation performance with low switching frequencies. To obtain the iterative equations for digital implementation of MPC, the mathematical models of (3) and (5) need to be discretized. Different from the space vector modulation based control schemes, the MPC control schemes could possess relatively higher sampling frequencies, although their switching frequencies could be low. Therefore, the requirement for discretization precision in MPC schemes is not as rigorous as that in the space vector modulation based control schemes. By considering the precision and the simplicity comprehensively, the first-order Euler method is utilized in this article, as shown in [17]

$$x(k+1) = Gx(k) + Hu(k) \tag{10}$$

$$V_n(k+1) = V_n(k) - \frac{T_s}{2C} \sum_x (1 - |S_x(k)|) i_x(k),$$

$$x \in \{a, b, c, d, e, f\} \tag{11}$$

where $G = I + T_s A$ and $H = T_s B$. I represents the identity matrix. T_s is the sampling period. The scripts (k) and $(k+1)$ denote the variable values sampled at instants kT_s and $(k+1)T_s$, respectively.
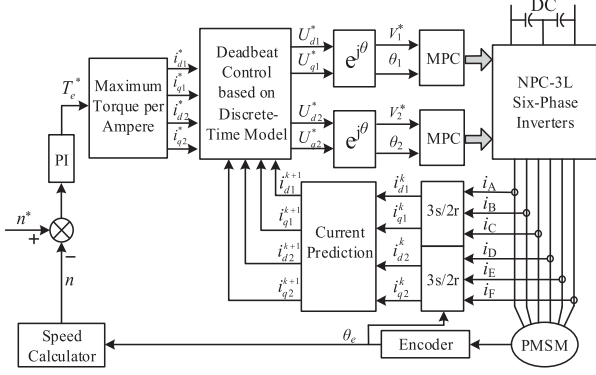
(a)
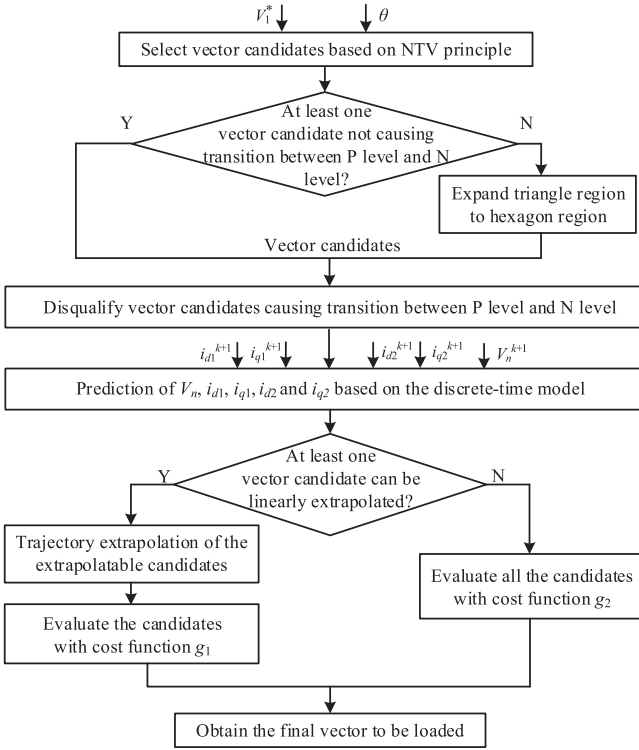
(b)

Fig. 3.   Diagram of the synchronous MPC scheme. (a) Overall control scheme. (b) Inner structure of the MPC blocks.

III. SYNCHRONOUS MPC

Fig. 3 shows the block diagram of the synchronous MPC scheme, where the sampling and the control algorithm are implemented synchronously. Therefore, the additional freedom in instant of sampling and control for dual three-phase motor drives has not been utilized, and the operation is similar to the conventional three-phase drives. As shown in Fig. 3(a), the torque reference is obtained from the PI control of rotor speed. The maximum torque per ampere (MTPA) method is utilized to generate the current references for FOC. Fig. 3(b) shows the inner structure of the MPC blocks of Fig. 3(a). To track the torque reference effectively while limiting the switching frequency, the control scheme is separated into two steps. The first step is to utilize the deadbeat control to generate the voltage references and select the voltage vector candidates with the NTV principle [18], [19]. As shown in Fig. 3(b), the second step is
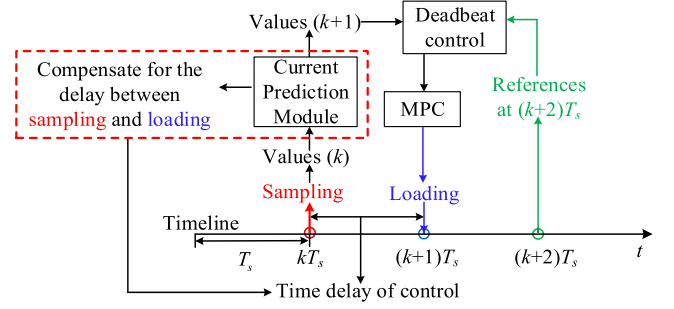

Fig. 4.   Diagram of compensation of control delay.

to evaluate the performance of the voltage vector candidates, where the trajectory extrapolation method is mainly used to solve the contradiction between the computational burden and prediction horizon. For the situation where no vector candidate satisfies the precondition of the trajectory extrapolation method, another cost function g_2 is used to evaluate the vector candidates. Furthermore, if all the vector candidates generated in the first step cause the switch transition between P level and N level, the vectors not causing the switch transition between P level and N level are selected as the new vector candidates.

A. Generation of Voltage Vector Candidates

In the first step, the voltage vector candidates are selected according to the voltage references calculated with the deadbeat control method. To compensate for the control delay, a current prediction module is utilized based on (10). Fig. 4 is used to exemplify the compensation of the control delay. As shown in Fig. 4, the control scheme selects the loaded vector based on the references at instant $(k+2)T_s$ and the initial values of variables at instant $(k+1)T_s$. Hence, there exists a time delay of T_s between the sampling instant and the loading instant. In this article, this time delay is compensated by the current prediction module, such that the deadbeat control is executed with the predicted values at instant $(k+1)T_s$ rather than the sampled values at instant kT_s.

Then, the current references generated by MTPA are set to be the desired currents at instant $(k+2)T_s$. With deadbeat control, the solutions are the voltages ensuring the currents at instant $(k+2)T_s$ to equal the current references exactly. So, the voltage solutions are set as the voltage references. The concrete implementation of deadbeat control is shown in

$$
\begin{cases}
u_{d1}{}^* = L_d(i_{d1}{}^* - i_{d1}(k+1))/T_s + L_{dm}(i_{d2}{}^* - i_{d2}(k+1))/T_s \\
\quad - \omega(k)L_q i_{q1}(k+1) - \omega(k)L_{qm}i_{q2}(k+1) + R_s i_{d1}(k+1) \\
u_{q1}{}^* = L_q(i_{q1}{}^* - i_{q1}(k+1))/T_s + L_{qm}(i_{q2}{}^* - i_{q2}(k+1))/T_s \\
\quad + \omega(k)L_d i_{d1}(k+1) + \omega(k)\psi_f + \omega(k)L_{dm}i_{d2}(k+1) \\
\quad + R_s i_{q1}(k+1) \\
u_{d2}{}^* = L_d(i_{d2}{}^* - i_{d2}(k+1))/T_s + L_{dm}(i_{d1}{}^* - i_{d1}(k+1))/T_s \\
\quad - \omega(k)L_q i_{q2}(k+1) - \omega(k)L_{qm}i_{q1}(k+1) \\
\quad + R_s i_{d2}(k+1) \\
u_{q2}{}^* = L_q(i_{q2}{}^* - i_{q2}(k+1))/T_s + L_{qm}(i_{q1}{}^* - i_{q1}(k+1))/T_s \\
\quad + \omega(k)L_d i_{d2}(k+1) + \omega(k)\psi_f + \omega(k)L_{dm}i_{d1}(k+1) \\
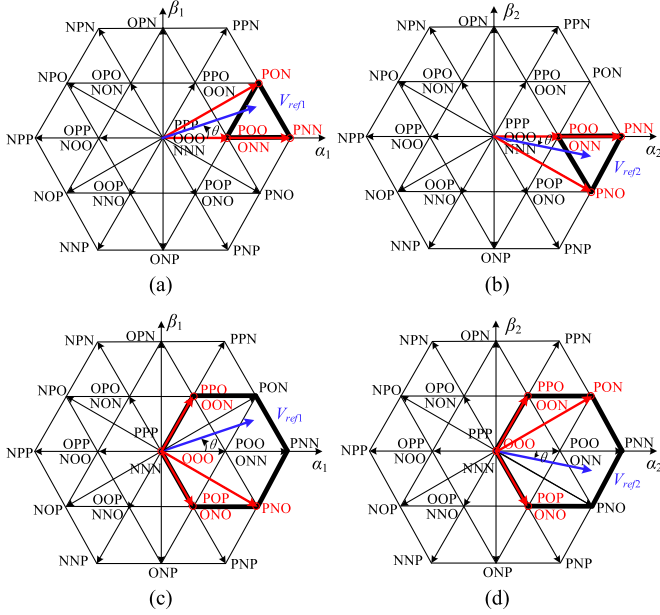\quad + R_s i_{q2}(k+1)
\end{cases}
$$
(12)

Fig. 5. Diagram of space voltage vector distribution in two NPC-3L inverters. (a) Triangle region of the first inverter. (b) Triangle region of the second inverter. (c) Hexagon region of the first inverter. (d) Hexagon region of the second inverter.

$$\begin{cases} i_{d1}{}^* = i_{d2}{}^* = \dfrac{1}{2} i_d{}^* \\ i_{q1}{}^* = i_{q2}{}^* = \dfrac{1}{2} i_q{}^* \end{cases} \qquad (13)$$

where $i_d{}^*$ and $i_q{}^*$ are the d-axis and q-axis current references obtained from MTPA, respectively. $u_{d1}{}^*$, $u_{q1}{}^*$, $i_{d1}{}^*$, and $i_{q1}{}^*$ are the d-axis and q-axis voltage references and current references for the first winding, respectively, whereas $u_{d2}{}^*$, $u_{q2}{}^*$, $i_{d2}{}^*$, and $i_{q2}{}^*$ are the d-axis and q-axis voltage references and current references for the second winding, respectively. With the voltage references, the vector candidates are selected with the following two steps.

Step 1: The two sets of NPC-3L inverters are considered on separate synchronous frames. Taking $\alpha_1\beta_1$-axis as the example, the corresponding NPC-3L inverter has the distribution of voltage vectors as shown in Fig. 5(a). The plane has been separated into 24 small regions. According to the NTV principle, the vector candidates are located on three corners of the triangle containing V_{ref1}. For example, when the location of V_{ref1} is located as shown in Fig. 5(a), the vector candidates are PNN, POO, ONN, and PON for the first set of NPC-3L inverter, which have been marked in red. Similarly, the vector candidates of the second inverter in Fig. 5(b) are POO, ONN, PNO, and PNN for the second set of NPC-3L inverter. It should be noted that the vector candidates causing the switch transition between P level and N level are required to be disqualified, as shown in the flowchart in Fig. 3(b). Suppose all the vector candidates are disqualified, the triangle region in the NTV principle is expanded to the hexagon region, as shown in Fig. 5(c) and (d). In Fig. 5(c), new vector candidates of the first inverter are PPO, OON, OOO, POP, ONO, and PNO. In Fig. 5(d), new vector candidates are PPO, OON, PON, OOO, POP, and ONO for the second inverter. These vector
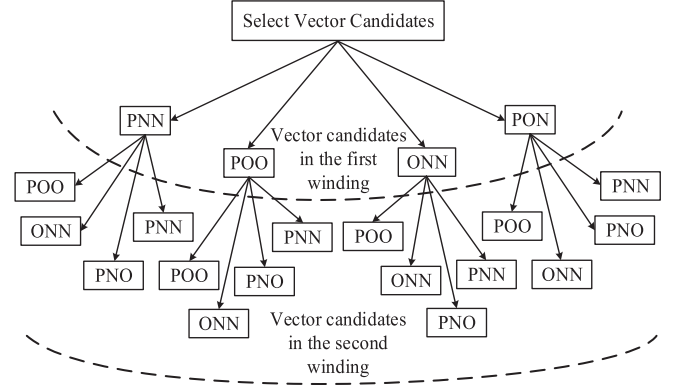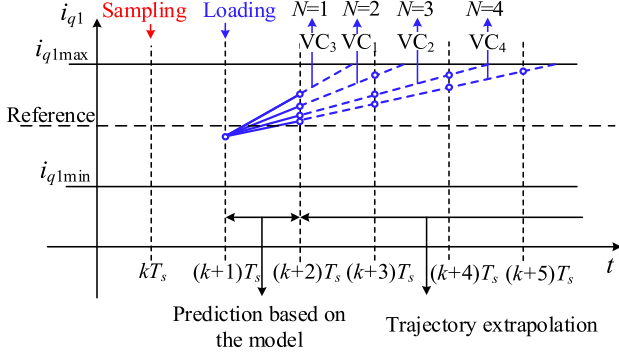

Fig. 6. Obtained 16 vector candidate sets of the two inverters.

candidates also require to be checked whether to cause switch transitions between P level and N level. The difference between the triangle region and the hexagon region is that there exists at least one vector without the switch transition between P level and N level in the hexagon region, whatever the previous switching state is.

Step 2: The vector candidates of the two inverters are combined, and they are used to construct the new vector candidate sets. The combination is conducted because there exist the cross-coupling effects between the two sets of windings in the dual three-phase PMSM, which means that the switch transition in an inverter for one winding will have impacts on the other winding. For example, it is assumed that the vector candidate sets in step 1 are {PNN, POO, ONN, PON} and {POO, ONN, PNO, PNN} for the first inverter and the second inverter, respectively. All possible combinations of these vector candidates are shown in Fig. 6. Therefore, there are totally 16 (4×4) different combinations of vector candidates with the first inverter and the second inverter. These 16 vector candidate combinations are the final candidate sets to be evaluated.

B. Evaluation of Voltage Vector Candidates

In the second step, the voltage vector candidate sets are evaluated. The overall evaluation process has been shown in Fig. 3(b). The values of $V_n(k+2)$, $i_{d1}(k+2)$, $i_{q1}(k+2)$, $i_{d2}(k+2)$, and $i_{q2}(k+2)$ are predicted with each voltage vector candidate, separately. With the specified hysteresis bounds, the trajectory extrapolation method is utilized to determine which voltage vector candidate set possesses the best performance at the next instant [16], [17]. Taking i_{q1} as an example, the trajectory extrapolation process is shown as Fig. 7. The dashed lines in blue represent the linear extrapolation process. If the predicted value $i_{q1}(k+2)$ at instant $(k+2)T_s$ is within the hysteresis bound of $(i_{q1\min}, i_{q1\max})$, the trajectory extrapolation is able to be conducted to find the length to hit the error bounds, which is defined as the length of extrapolation. As shown in Fig. 7, the extrapolation lengths of the four vector candidates VC_1, VC_2, VC_3, and VC_4 are equal to 2, 3, 1, and 4, respectively. The trajectory extrapolation processes of i_{d1}, i_{d2}, i_{q2}, and V_n are similar to the process of i_{q1}. Then, the smallest extrapolation length of i_{d1},

Fig. 7. Trajectory extrapolation process of i_{q1}.

Fig. 8. Control sequence comparison. (a) Synchronous control. (b) Proposed interleaved control.

i_{q1}, i_{d2}, i_{q2}, and V_n is defined as the final extrapolation length N of the corresponding vector candidate.

To evaluate the switching frequency, the number of commutations is defined for each vector candidate as follows:

$$n_s = \sum_x |S_x(k+1) - S_x(k)|, x \in \{a, b, c, d, e, f\}. \quad (14)$$

With the final extrapolation length N and the number of commutations n_s, the average switching frequency generated by the vector candidate set is $n_s/(24NT_s)$. Considering the sampling period T_s is constant, the cost function of the FCS-MPC is given as in the following equation:

$$g_1 = \frac{n_s}{N}. \quad (15)$$

If all the candidates have at least one variable with the predicted value at instant $(k+2)T_s$ beyond the given bound, the similar method as in [25] is used. The vector candidates will be evaluated by another cost function, which is given as the following equation:

$$g_2 = \sum_x \lambda_x g_x, x \in \{i_{d1}, i_{q1}, i_{d2}, i_{q2}, V_n\}$$
$$g_x = \begin{cases} x(k+2) - x_{\max}, x(k+2) > x_{\max} \\ x_{\min} - x(k+2), x(k+2) < x_{\min} \\ 0, x_{\min} \le x(k+2) \le x_{\max} \end{cases} \quad (16)$$
$$\lambda_x = \frac{1}{x_{\max} - x_{\min}}$$

where λ_{Vn}, λ_{id1}, λ_{iq1}, λ_{id2}, and λ_{iq2} are the weighting factors for the control of the midpoint voltage, d_1-axis current, q_1-axis current, d_2-axis current, and q_2-axis current, respectively, and $x_{\max}$ and $x_{\min}$ are the maximum value and the minimum value within the error bounds of the corresponding variables, separately. The weighting factors are set to be the reciprocal of the difference between the predefined upper and lower bounds, i.e., the widths of the hysteresis bounds, to normalize the variables and ensure the comparability between these variables. In this article, the hysteresis bounds of current variables are set to be $\pm 10\%$ of the amplitude of the current reference in the corresponding three-phase winding. Therefore, the weighting factors for the currents are set as: $\lambda_{id1} = 1/(0.2I_1^*)$, $\lambda_{iq1} = 1/(0.2I_1^*)$, $\lambda_{id2} = 1/(0.2I_2^*)$, $\lambda_{iq2} = 1/(0.2I_2^*)$, where $I_1^* = \sqrt{i_{d1}^{*2} + i_{q1}^{*2}}$ and $I_2^* = \sqrt{i_{d2}^{*2} + i_{q2}^{*2}}$. The hysteresis bound for the midpoint
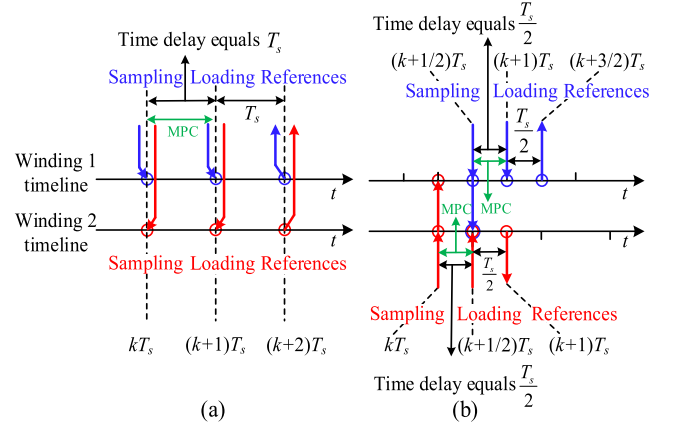
voltage is set to be $\pm 0.5\%$ of the dc-link voltage. Therefore, the weighting factor for the midpoint voltage is given as $\lambda_{Vn} = 1/(0.01U_{dc})$.

IV. INTERLEAVED MPC

Different from the synchronous control with simultaneous sampling and control for two sets of three-phase windings, the interleaved sampling and control scheme is proposed in this section, where more degrees of control freedom of dual three-phase motor drives are fully utilized. With the proposed interleaved scheme, the equivalent frequency of sampling and implementation of the control algorithm is increased. Therefore, both the steady-state and dynamic control performance of the motor drive will be improved significantly.

A. Control Sequence of Interleaved Sampling and Control

Fig. 8 is utilized to exemplify and compare the control sequence of the synchronous control method and the proposed interleaved control method. With synchronous control in Fig. 8(a), the variables of both windings are sampled at instant kT_s and the vectors of the two windings are loaded simultaneously at instant $(k+1)T_s$. Additionally, the state variables are expected to track the reference values at instant $(k+2)T_s$. The feature of the synchronous method is that the sampling and loading instants of the two windings are simultaneous and the whole prediction horizon is equal to $2T_s$. One T_s in the prediction horizon is to compensate for the control delay and the other T_s in the prediction horizon is to evaluate the vector candidates.

On the other hand, with the interleaved method in Fig. 8(b), the state variables of the first winding are sampled at instant $(k+1/2)T_s$ and the selected vector is loaded at instant $(k+1)T_s$, whereas the state variables of the second winding are sampled at instant kT_s and the selected vector is loaded at instant $(k+1/2)T_s$. The feature of the proposed interleaved method is that the sampling and loading instants of the two three-phase windings are interleaved by $T_s/2$, and the whole prediction horizon is equal to T_s instead of $2T_s$ with the synchronous control. In the whole prediction horizon of T_s with the interleaved control,
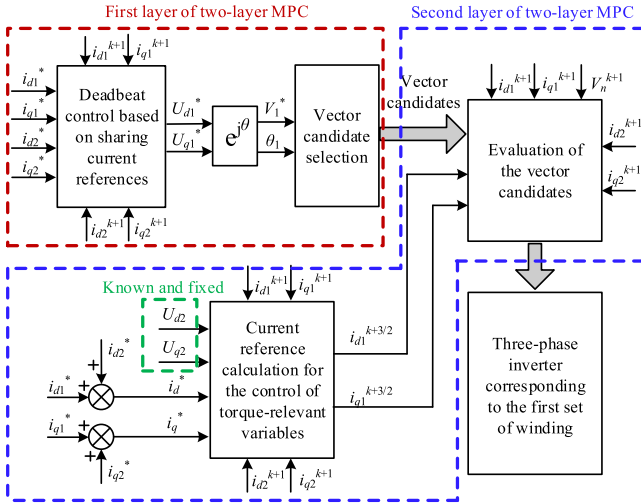
Fig. 9. Block diagram for the implementation of the two-layer MPC.

$0.5T_s$ is for the compensation of the control delay and $0.5T_s$ is for evaluation of the vector candidates. The detailed principle and implementation of the proposed interleaved MPC scheme with the control sequence of Fig. 8(b) are presented in the following part of this section.

B. MOOP and Two-Layer MPC in Interleaved Control

Different from synchronous control, the proposed interleaved control method only changes the switching state of a single three-phase inverter during each sampling period. The switching state of the other inverter is determined in the previous and the next sampling period. Therefore, as aforementioned, there exists the MOOP, where the dimension of objective variables exceeds the dimension of controllable variables.

To solve the MOOP, a two-layer MPC is proposed in this article based on SMPC in [21]–[23] and the feature of the dual three-phase drives. The first layer is to ensure the torque-irrelevant variables roughly within the tolerant range, and the second layer is to execute the optimal control of the torque-relevant variables. Considering the relationship between the dual dq-frame and the VSD decoupling method, the torque-relevant variables can be regarded as the sum of d_1-axis and d_2-axis currents, and the sum of q_1-axis and q_2-axis currents.

The flowchart of the two-layer MPC in the interleaved control is almost the same as Fig. 3(b), except for the reduced dimensions in the cost function g_2 and the criterion for selecting and evaluating vector candidates. The first layer of MPC is embedded in the selection of the vector candidates, and the second layer of MPC is the evaluation of the vector candidates. The implementation of two-layer MPC is illustrated in the following content of this part.

Taking the sampling and control at instant $(k+1/2)T_s$ in Fig. 8(b) as an example, the implementation of the two-layer MPC is presented in Fig. 9. It indicates that the control scheme for the two-layer MPC is similar to that of the synchronous MPC scheme in Fig. 3(b). The deadbeat control calculation is implemented to determine the vector candidates with the same

method in Fig. 5. Then, the evaluation of the vector candidates is conducted, where the cost function of g_1 or g_2 is chosen, depending on whether there exists a vector candidate to be linearly extrapolated. As shown in Fig. 8(b), the new vector of the second three-phase winding is loaded at instant $(k+1/2)T_s$ and the switching state of this corresponding inverter is kept unchanged until the instant $(k+3/2)T_s$. Therefore, the d_2-axis voltage U_{d2} and the q_2-axis voltage U_{q2} are fixed and known during the control horizon of the first three-phase winding, i.e., the period from instant $(k+1/2)T_s$ to instant $(k+3/2)T_s$. Consequently, the 2-D desired current references, namely $i_{d1}^{k+3/2}$ and $i_{q1}^{k+3/2}$, are used in the control horizon of the first three-phase winding with the proposed interleaved MPC. The desired current references of $i_{d1}^{k+3/2}$ and $i_{q1}^{k+3/2}$ are calculated from the total d-axis and the total q-axis current references. On the other hand, the synchronous MPC scheme has to track the 4-D current references.

1) First Layer of Two-Layer MPC: In the first layer, the objective is to obtain the desired voltage reference for making the difference between the d_1-axis and the d_2-axis currents and the difference between the q_1-axis and q_2-axis currents zero. Meanwhile, the deadbeat control is used in the first layer to regulate the sum of the d_1-axis and d_2-axis currents, and the sum of the q_1-axis and q_2-axis currents to ensure the control performance of the torque-relevant variables. In Fig. 8(b), the sampling and implementation of the control algorithm of winding 1 at instant $(k+1/2)T_s$ are used as an example. According to the discrete-time model in (10), the ideal expressions for the voltage references u_{d1}^*, u_{q1}^*, u_{d2}^*, and u_{q2}^* are calculated as follows:

$$
\begin{cases}
u_{d1}^* = R_s i_{d1}(k+1) + L_d(i_{d1}^* - i_{d1}(k+1))/(T_s/2) \\
\quad - \omega(k+1/2)L_{qm}i_{q2}(k+1) \\
\quad + L_{dm}(i_{d2}^* - i_{d2}(k+1))/(T_s/2) - \omega(k+1/2)L_q i_{q1}(k+1) \\
u_{q1}^* = R_s i_{q1}(k+1) + L_q(i_{q1}^* - i_{q1}(k+1))/(T_s/2) \\
\quad + \omega(k+1/2)L_{dm}i_{d2}(k+1) \\
\quad + L_{qm}(i_{q2}^* - i_{q2}(k+1))/(T_s/2) + \omega(k+1/2)L_d i_{d1}(k+1) \\
\quad + \omega(k+1/2)\psi_f \\
u_{d2}^* = R_s i_{d2}(k+1) + L_d(i_{d2}^* - i_{d2}(k+1))/(T_s/2) \\
\quad - \omega(k+1/2)L_{qm}i_{q1}(k+1) \\
\quad + L_{dm}(i_{d1}^* - i_{d1}(k+1))/(T_s/2) - \omega(k+1/2)L_q i_{q2}(k+1) \\
u_{q2}^* = R_s i_{q2}(k+1) + L_q(i_{q2}^* - i_{q2}(k+1))/(T_s/2) \\
\quad + \omega(k+1/2)L_{dm}i_{d1}(k+1) + L_{qm}(i_{q1}^* - i_{q1}(k+1))/(T_s/2) \\
\quad + \omega(k+1/2)L_d i_{d2}(k+1) \\
\quad + \omega(k+1/2)\psi_f
\end{cases}
\tag{17}
$$

$$
\begin{cases}
i_{d1}^* = i_{d2}^* = \dfrac{1}{2}i_d^* \\
i_{q1}^* = i_{q2}^* = \dfrac{1}{2}i_q^*.
\end{cases}
\tag{18}
$$

It should be noted that u_{d2} and u_{q2} have been determined and updated at instants kT_s and $(k+1/2)T_s$, respectively, and cannot be changed until instant $(k+3/2)T_s$. Therefore, the ideal reference values of u_{d2}^* and u_{q2}^* in (17) are not able to be implemented. However, the high sampling frequency in the FCS-MPC scheme ensures there is no significant difference between the values of u_{d2} and u_{q2} determined at instant kT_s and the

reference values of u_{d2}^* and u_{q2}^* derived in (17). Therefore, it is reasonable to utilize u_{d1}^* and u_{q1}^* in (17) to delimit the region for the selection of vector candidates, roughly. It can be seen from (17) and (18) that, the deadbeat calculation in the interleaved control is almost the same as the synchronous control, except for the voltage references reduced to be 2-D and the discrete step is shortened to $T_s/2$.

Based on the voltage references, the NTV principle is utilized to generate the vector candidates. With the interleaved control sequence, it is not necessary to combine the vector candidates of two sets of three-phase windings. Therefore, the proposed interleaved control can reduce the number of vector candidates significantly and simplify practical algorithm implementation.

2) Second Layer of Two-Layer MPC: The objective of the second layer is to control the sum of the d_1-axis and the d_2-axis currents, and the sum of the q_1-axis and the q_2-axis currents for tracking the current references from MTPA. It is worth noting that, it is only necessary to select two variables from i_{d1}, i_{q1}, i_{d2}, and i_{q2} as the objective variables with the interleaved control sequence. The other two variables will contribute naturally to tracking the current references from MTPA. In this article, the objective variables selected for winding 1 are i_{d1} and i_{q1}, whereas i_{d2} and i_{q2} are selected as the objective variables for winding 2. In Fig. 8(b), the sampling and the implementation of the control algorithm for winding 1 at instant $(k+1/2)T_s$ are used as an example. Due to the interleaved control sequence, the switching state of the second inverter is known and fixed from instant $(k+1/2)T_s$ to $(k+3/2)T_s$, and the values of u_{d2} and u_{q2} are also known and fixed. Therefore, in the instant between $(k+1)T_s$ and $(k+3/2)T_s$, there are the following relationships in (19) with the fixed voltage values u_{d2} and u_{q2}:

$$
\begin{cases}
u_{d2} = R_s i_{d2}(k+1) + L_d(i_{d2}(k+3/2) - i_{d2}(k+1))/(T_s/2) \\
\quad + L_{dm}(i_{d1}(k+3/2) - i_{d1}(k+1))/(T_s/2) \\
\quad - \omega(k+1/2)L_q i_{q2}(k+1) - \omega(k+1/2)L_{qm} i_{q1}(k+1) \\
u_{q2} = R_s i_{q2}(k+1) + L_q(i_{q2}(k+3/2) - i_{q2}(k+1))/(T_s/2) \\
\quad + L_{qm}(i_{q1}(k+3/2) - i_{q1}(k+1))/(T_s/2) \\
\quad + \omega(k+1/2)L_d i_{d2}(k+1) + \omega(k+1/2)\psi_f + \omega(k+1/2) \\
L_{dm} i_{d1}(k+1).
\end{cases}
\tag{19}
$$

On the other hand, the control objectives of torque-relevant variables are shown in the following equation:

$$
\begin{cases}
i_{d1}(k+3/2) + i_{d2}(k+3/2) = i_d^* \\
i_{q1}(k+3/2) + i_{q2}(k+3/2) = i_q^*.
\end{cases}
\tag{20}
$$

In (19) and (20), the values of $i_{d1}(k+1)$, $i_{q1}(k+1)$, $i_{d2}(k+1)$, and $i_{q2}(k+1)$ are predicted based on the discrete-time model (10), with the sampled current values at instant $(k+1/2)T_s$ and the values of u_{d1}, u_{q1}, u_{d2}, and u_{q2} determined in the previous sampling periods. Therefore, it is observed that $i_{d1}(k+3/2)$, $i_{q1}(k+3/2)$, $i_{d2}(k+3/2)$, and $i_{q2}(k+3/2)$ are the four variables to be solved in the 4-D equation sets in (19) and (20). The solutions
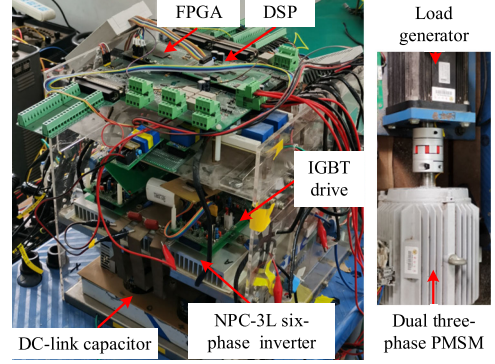

Fig. 10. Photograph of the experimental setup.

to $i_{d1}(k+3/2)$ and $i_{q1}(k+3/2)$ are given in the following equation:

$$
\begin{cases}
i_{d1}(k+3/2) = (L_d i_{d2}(k+1) + L_{dm} i_{d1}(k+1) - L_d i_d^* \\
\quad + u_{d2}T_s/2 \\
\quad - R_s T_s i_{d2}(k+1)/2 + \omega(k+1/2)L_q T_s i_{q2}(k+1)/2 \\
\quad + \omega(k+1/2)L_{qm}T_s i_{q1}(k+1)/2)/(L_{dm} - L_d) \\
i_{q1}(k+3/2) = (L_{qm} i_{q1}(k+1) + L_q i_{q2}(k+1) \\
\quad - T_s \omega(k+1/2)\psi_f/2 \\
\quad - L_q i_q^* - R_s T_s i_{q2}(k+1)/2 - \omega(k+1/2)L_d T_s i_{d2}(k+1)/2 \\
\quad - \omega(k+1/2)L_{dm}T_s i_{d1}(k+1)/2 + u_{q2}T_s/2)/(L_{qm} - L_q).
\end{cases}
\tag{21}
$$

With the result shown in (21), the vector candidates determined in the first layer are evaluated. The evaluation functions of the vector candidates are consistent with the synchronous control, except that the amount of control objectives is reduced. Taking the sampling and the implementation of the control algorithm in the first winding at instant $(k+1/2)T_s$ in Fig. 8(b) as an example, the cost function g_2 in the interleaved control scheme is shown in the following equation:

$$
\begin{aligned}
&g_2 = \sum_x \lambda_x g_x, x \in \{i_{d1}, i_{q1}, V_n\} \\
&g_x = \begin{cases}
x(k+2) - x_{\max}, x(k+2) > x_{\max} \\
x_{\min} - x(k+2), x(k+2) < x_{\min} \\
0, x_{\min} \le x(k+2) \le x_{\max}
\end{cases} \\
&\lambda_x = \frac{1}{x_{\max} - x_{\min}}
\end{aligned}
\tag{22}
$$

where the values of the weighting factors are set the same as those in (16), namely $\lambda_{id1} = 1/(0.2I_1^*)$, $\lambda_{iq1} = 1/(0.2I_1^*)$, and $\lambda_{Vn} = 1/(0.01U_{dc})$. Compared with the synchronous control, the computational burden in evaluating a single vector candidate in the interleaved control is relieved, since the control objectives are reduced from $\{V_n, i_{d1}, i_{q1}, i_{d2}, i_{q2}\}$ to $\{V_n, i_{d1}, i_{q1}\}$ with the proposed interleaved control.

V. EXPERIMENTAL VERIFICATION

The experiments are carried out on a laboratory prototype of NPC-3L inverter-fed dual three-phase PMSM drive to verify the effectiveness of the proposed interleaved control scheme. A photograph of the experimental setup is shown in Fig. 10. In the experiments, the control schemes are implemented by DSP TI-TMS320F28346 and field-programmable gate array (FPGA) Xilinx-Spartan6 XC6SLX25. The DSP performs the control

TABLE I
KEY PARAMETERS OF EXPERIMENTAL SETUP

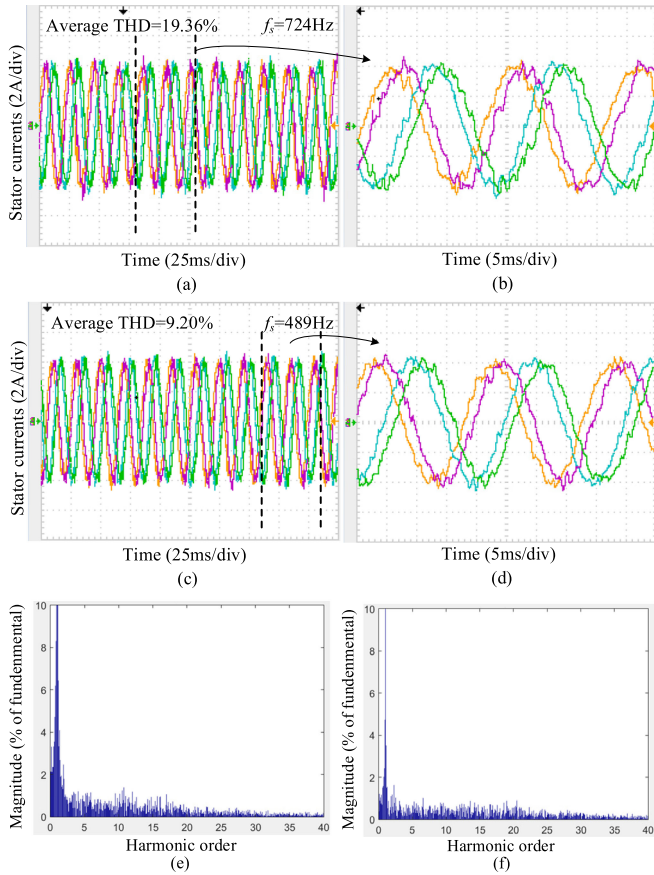| Name	Value
Pole pair number	4
q-axis inductance	13.0mH
d-axis inductance	10.0 mH
Leakage inductance	5.0 mH
PM flux (amplitude)	0.08 Wb
Stator resistance	0.225 Ω
DC-link capacitance	4000 μF
Vector selection frequency	7.5 kHz
DC-link voltage	100V

Fig. 11. Stator currents of phases A, B, D, and E. (a) Current waveforms with the synchronous MPC scheme. (b) Zoomed current waveforms with the synchronous MPC scheme. (c) Current waveforms with the proposed interleaved MPC scheme. (d) Zoomed current waveforms with the proposed interleaved MPC scheme. (e) Spectrum for the current of phase A with the synchronous MPC scheme. (f) Spectrum for the current of phase A with the interleaved MPC scheme.
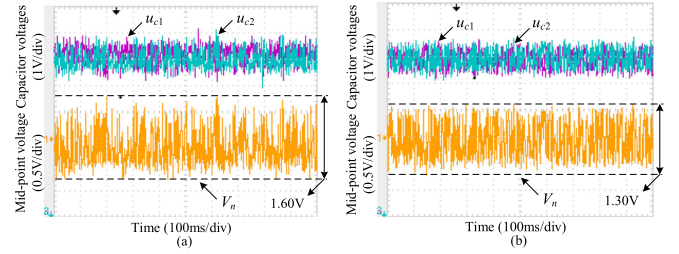

Fig. 12. DC-link capacitor voltages and midpoint voltage. (a) Synchronous MPC. (b) Proposed interleaved MPC.
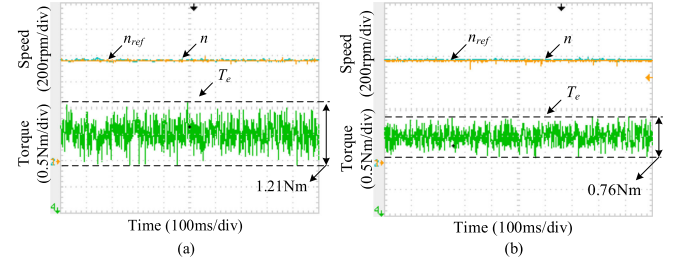

Fig. 13. Speed and torque waveforms. (a) Synchronous MPC. (b) Proposed interleaved MPC.
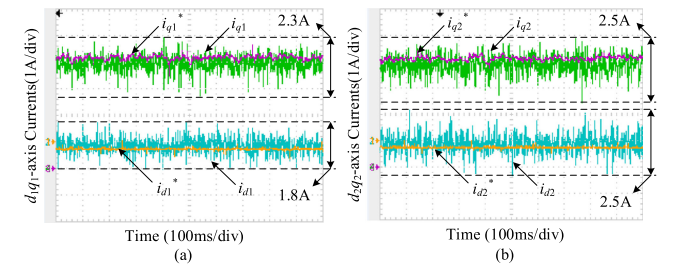

Fig. 14. Steady-state current waveforms with the synchronous MPC scheme. (a) d_1-axis and q_1-axis currents. (b) d_2-axis and q_2-axis currents.
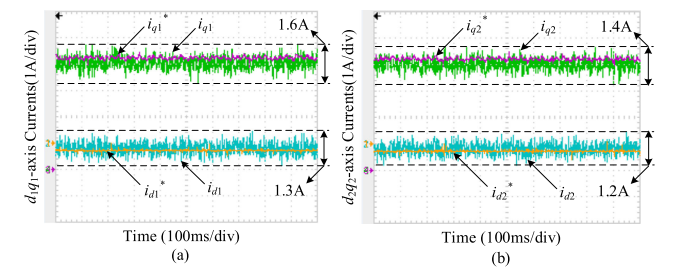

Fig. 15. Steady-state current waveforms with the interleaved MPC scheme. (a) d_1-axis and q_1-axis currents. (b) d_2-axis and q_2-axis currents.

algorithm and the FPGA generates the control signals of the inverters. A three-phase permanent-magnet generator is coupled to the dual three-phase PMSM to act as the load. The key system parameters are listed in Table I.

First, the steady-state control performance of the synchronous MPC and the proposed interleaved MPC under the 50 Hz fundamental electric frequency is compared in Figs. 11–17. Fig. 11 compares the waveforms of the stator currents of phases A,

B, D, and E with these two control schemes. Fig. 11(a) and (c) shows the current waveforms of 12.5 fundamental cycles with the synchronous and with the interleaved MPC schemes, respectively. Fig. 11(b) and (d) shows the corresponding zoomed waveforms of 2.5 fundamental cycles. At first, the switching frequency is calculated for each power switch by counting the number of switching actions in 1 s. Then, the average switching frequency is obtained by averaging the switching
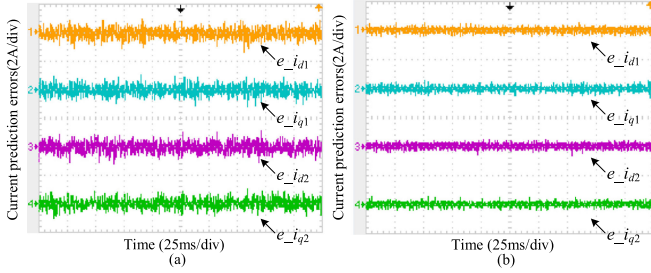
Fig. 16. Prediction errors of i_{d1}, i_{q1}, i_{d2}, and i_{q2}. (a) Synchronous MPC scheme. (b) Interleaved MPC scheme.
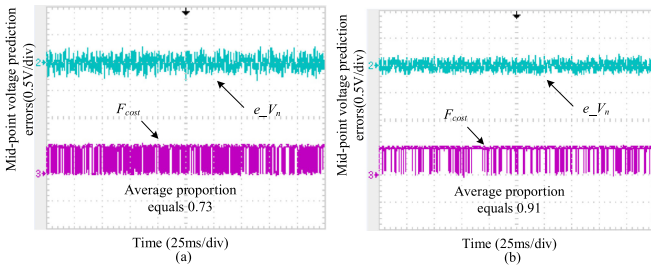

Fig. 17. Comparison of e_V_n and F_{cost}. (a) Synchronous MPC scheme. (b) Proposed interleaved MPC scheme.

frequencies in 5 s [26]. The average switching frequencies of the synchronous control and the interleaved control are 724 and 489 Hz, respectively. The switching frequency is an average value because it usually fluctuates within a small range with the MPC control scheme. It is observed that the average switching frequency is reduced by 32.5% by using the interleaved control scheme, compared with the synchronous control. Moreover, the total harmonic distortion (THD) value for each phase current is calculated with the measured data of 12 fundamental cycles. Specifically, the THD values of the currents in phases A, B, D, and E using the synchronous MPC scheme are 17.97%, 20.60%, 19.87%, and 18.98%, respectively. The corresponding average THD value is 19.36%. On the other hand, the THD values of the currents in phases A, B, D, and E using the interleaved MPC scheme are 9.34%, 8.89%, 9.69%, and 8.86%, respectively. The corresponding average THD value is 9.20%. Moreover, the current spectrums of phase A using the two control schemes are shown in Fig. 11(e) and (f), respectively, where the flat spectrum is observed. The reason is due to the variable switching frequencies using MPC schemes, and the current spectrum does not possess characteristic harmonics [15]. From Fig. 11(e) and (f), it can be observed that the current harmonics using the interleaved MPC scheme are less due to the reduced current ripples, compared to the synchronous MPC scheme. Therefore, the proposed interleaved control offers better THD performance while using lower switching frequencies.

Fig. 12 compares the dc-link capacitor voltages and the midpoint voltage fluctuation waveforms. The waveforms on the top are voltages of the upper and the lower capacitors in dc link. The waveforms at the bottom show the midpoint voltage waveforms. The value of $V_{n\max}$ is set to 0.5%U_{dc}, equaling

0.5 V. It is observed that fluctuations of the midpoint voltage using the synchronous control and the interleaved control are 1.60 and 1.30 V, respectively. Since the interleaved control possesses the smaller control delay, the interleaved control can suppress the fluctuation faster when the midpoint voltage is approaching the hysteresis bounds. Fig. 13 shows the steady-state speed and torque waveforms. It can be observed that both the two control schemes possess satisfactory tracking performance. The peak-to-peak torque ripples of the synchronous control and the interleaved control are 1.21 and 0.76 N·m, respectively. Figs. 14 and 15 show the steady-state waveforms of d_1-axis current, q_1-axis current, d_2-axis current, and q_2-axis current. It is observed that these currents can track the reference values well with both of the two control schemes. As shown in Figs. 14 and 15, the peak-to-peak values of tracking errors for the d_1-axis, the q_1-axis, the d_2-axis, and the q_2-axis current are 2.3, 1.8, 2.5, and 2.5 A, respectively, with the synchronous control, whereas those values are 1.6, 1.3, 1.4, and 1.2 A, respectively, with the interleaved control. Therefore, Figs. 11–15 verify that the interleaved control scheme possesses significant superiority in steady-state control performance with the higher equivalent frequency of sampling and control for the drive system.

Fig. 16(a) and (b) shows the experimental results of the prediction errors of i_{d1}, i_{q1}, i_{d2}, and i_{q2} with the synchronous MPC scheme and the interleaved MPC scheme, respectively. The symbols of e_i_{d1}, e_i_{q1}, e_i_{d2}, and e_i_{q2} denote the prediction errors of i_{d1}, i_{q1}, i_{d2}, and i_{q2}, respectively. The prediction horizon includes two parts: the first one is from the sampling instant to the loading instant, and the second one is from the loading instant to the final prediction instant. Therefore, the total prediction horizon for the synchronous MPC scheme is $2T_s$, as shown in Fig. 8(a). On the other hand, the total prediction horizon for the interleaved MPC scheme is T_s, as shown in Fig. 8(b). Since the total prediction horizon is reduced by half, the current prediction errors with the interleaved MPC scheme are smaller than those with the synchronous MPC scheme, as shown in Fig. 16. Fig. 17 compares the experimental results of the midpoint voltage prediction and proportions for the choice between the two cost functions g_1 and g_2 with the synchronous MPC scheme and the proposed interleaved MPC scheme. e_V_n denotes the error of the midpoint voltage prediction within the total prediction horizon. As shown in Fig. 17(a) and (b), it is observed that the prediction error with the proposed interleaved MPC scheme is smaller than that with the synchronous MPC scheme. Therefore, the control performance of the midpoint voltage fluctuation is better with the proposed interleaved MPC scheme. To further illustrate the reason for the interleaved MPC scheme with the lower switching frequency, a flag, namely F_{cost}, is used to indicate the choice between the two cost functions g_1 and g_2. As shown in Fig. 17, the high level of F_{cost}, namely the value of 1, indicates that the cost function g_1 is used to determine the final selected vector. On the other hand, the low level of F_{cost}, namely the value of 0, indicates that the cost function g_2 is used to determine the final selected vector. In the experiments, the average values of F_{cost} are 0.73 and 0.91 with the synchronous MPC scheme and with the proposed interleaved MPC scheme, respectively. It indicates that g_1 is utilized more
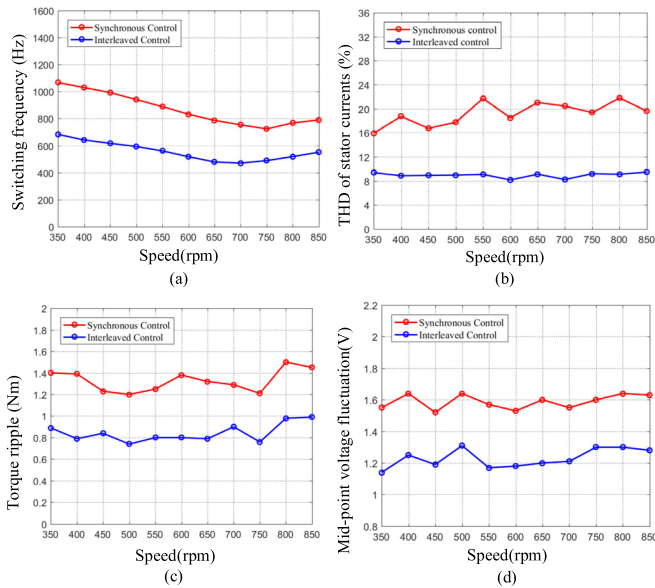
Fig. 18. Experimental results of the synchronous MPC scheme and the interleaved MPC scheme under different speed conditions. (a) Switching frequencies. (b) THD values. (c) Torque ripples. (d) Midpoint voltage fluctuation.
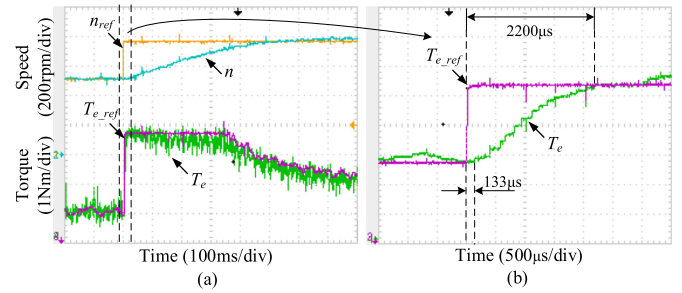

Fig. 19. Dynamic control performance of the synchronous MPC scheme. (a) Speed and torque waveforms. (b) Zoomed dynamic response of torque.
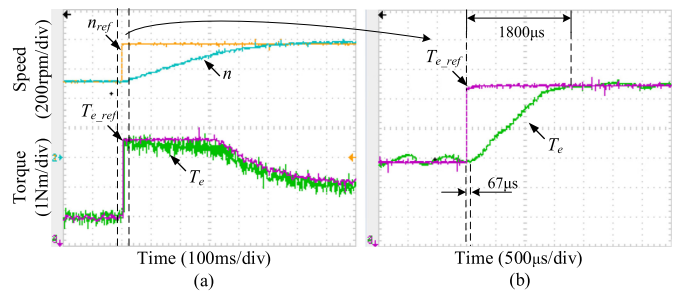

Fig. 20. Dynamic control performance of the interleaved MPC scheme. (a) Speed and torque waveforms. (b) Zoomed dynamic response of torque.

frequently with the interleaved MPC scheme, which contributes to the more effective reduction in the switching frequency.

Second, the experimental results of the switching frequencies, THD values, torque ripples, and midpoint voltage fluctuation of the two control schemes are compared under different speeds in Fig. 18. Fig. 18(a) shows that the switching frequency of the interleaved control is smaller than the synchronous control under all tested speeds. Meanwhile, Fig. 18(b) shows that the interleaved control offers the lower THD values of stator currents compared to the synchronous control. Fig. 18(c) shows the torque ripple of the drive under different speeds. It is observed that the torque ripple of the synchronous control is around 1.4 N·m, whereas the torque ripple of the interleaved control is approximated to be 0.9 N·m. Fig. 18(d) shows the experimental results of the midpoint voltage fluctuation. In Fig. 18(d), it is observed that the midpoint voltage fluctuation of the synchronous control is around 1.60 V, whereas the fluctuation amplitudes of the interleaved control are roughly around 1.25 V. Therefore, the experimental results in Fig. 18 have verified the superiority of the proposed interleaved MPC scheme in steady-state control performance with the lower switching frequencies.

Third, the dynamic control performance of the synchronous MPC and the proposed interleaved MPC is compared in Figs. 19 and 20. The given speed reference switches between 500 and 750 r/min. It can be observed in Figs. 19(a) and 20(a) that both the torque and the speed can track their reference values accurately and quickly with the two control schemes. Figs. 19(b) and 20(b) are the zoomed torque responses. The time of torque response is 2200 μs with the synchronous control, whereas the torque response is 1800 μs with the interleaved control, which are shown in Figs. 19(b) and 20(b), respectively. Moreover, the delayed time for the torque to start rising is reduced by half in the interleaved control due to its doubled equivalent switching frequency. The delayed time with the synchronous control is

133 μs, corresponding to the sampling frequency 7.5 kHz. On the other hand, the delayed time with the interleaved control is 67 μs, corresponding to the doubled sampling frequency of 15 kHz. Besides, it takes the proposed interleaved control the rise time of 1800 μs to track the sudden change of torque reference, whereas the time is 2200 μs with the synchronous control. So, the interleaved control offers less track time for torque response.

Lastly, the execution time of the synchronous control and the proposed interleaved control is compared in Fig. 21. The DSP program can be divided into four main parts, namely the analog-to-digital (AD) conversion, the delay compensation, the MPC algorithm, and the loading of the final vector. The programs of the two control schemes are almost the same. Therefore, the execution time of these three parts is the same with the two control schemes. The execution time of the MPC algorithm with the synchronous control scheme is 95.69 μs, whereas the execution time of the MPC algorithm with the interleaved control scheme is 20.28 μs for each three-phase winding, and thus 40.56 μs for the two three-phase windings totally. Consequently, the total execution times to control two three-phase windings are 116.56 and 82.30 μs with the synchronous control and the interleaved control, respectively. The main reason for the reduction of computational burden lies in that only voltage vectors of one three-phase inverter are required to be evaluated, and the switching state of the other inverter is fixed for each time of sampling and calculation with the proposed interleaved control. Therefore, the cross traversal of vector candidates between the two three-phase inverters can be avoided. It contributes to the reduction of the computational burden for the interleaved MPC scheme compared to the conventional synchronous MPC
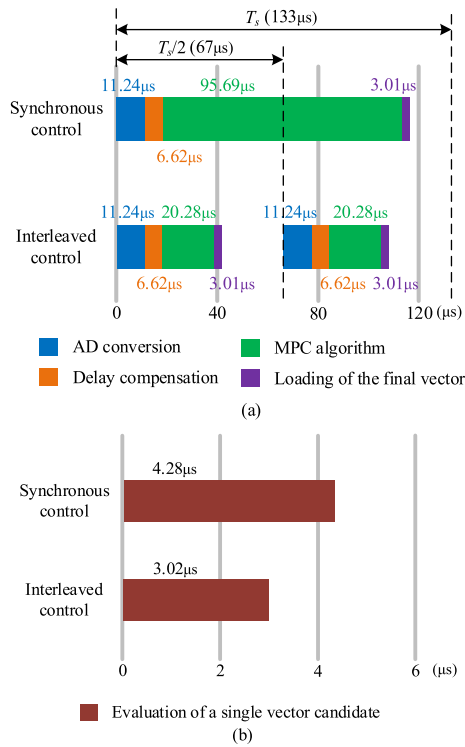
Fig. 21. Execution time of the synchronous control and the proposed interleaved control. (a) Whole program. (b) Evaluation of a single vector candidate.

scheme. Apart from that, Fig. 21(b) shows another reason for the reduction of the computational burden, where the execution time for the evaluation of a single vector candidate is less with the proposed interleaved MPC scheme. The synchronous control needs 4.28 μs, whereas the interleaved control requires 3.02 μs due to the reduced dimension of control objectives. Therefore, the computational burden of the proposed interleaved control is still reduced, although it requires to implement the AD conversion, the delay compensation, the MPC and load of final vector twice during a whole period for dual three-phase windings.

VI. Conclusion

In this article, the MPC scheme has been studied for the NPC-3L inverter-fed dual three-phase PMSM drives with low switching frequencies. The dual *dq*-frame based FOC is adopted to control each of the three-phase winding on the separate synchronous frames. Compared to synchronous control, the proposed interleaved control methods possess the following advantages.

1) With the interleaved sampling and control strategies, both the delay in digital implementation and the prediction horizon are reduced by half, which contributes to improving the prediction accuracy of the control algorithm.
2) The proposed two-layer MPC in the interleaved control doubles the equivalent frequency of sampling and control for the whole drive. Therefore, the steady-state and the dynamic control performance of the drive system are enhanced.

3) The proposed interleaved control avoids the cross traversal of vector candidates between two sets of windings, which simplifies evaluation functions of the vector candidates, and contributes to the decrement in the calculation burden.

The experiments have been carried out to verify that the proposed interleaved control can offer better performance in harmonics, torque ripple, midpoint voltage fluctuation, and dynamic response while maintaining the lower switching frequency.

References

[1] J. Rodríguez, S. Bernet, B. Wu, J. O. Pontt, and S. Kouro, "Multi-level voltage-source-converter topologies for industrial medium-voltage drives," *IEEE Trans. Ind. Electron.*, vol. 54, no. 6, pp. 2930–2945, Dec. 2007.

[2] Z. Wang, X. Wang, M. Cheng, and Y. Hu, "Comprehensive investigation on remedial operation of switch faults for dual three-phase PMSM drives fed by T-3L inverters," *IEEE Trans. Ind. Electron.*, vol. 65, no. 6, pp. 4574–4587, Jun. 2018.

[3] F. Barrero and M. J. Duran, "Recent advances in the design, modeling, and control of multiphase machines—Part I," *IEEE Trans. Ind. Electron.*, vol. 63, no. 1, pp. 449–458, Jan. 2016.

[4] B. Wu, D. Xu, J. Ji, W. Zhao, and Q. Jiang, "Field-oriented control and direct torque control for a five-phase fault-tolerant flux-switching permanent-magnet motor," *Chin. J. Elect. Eng.*, vol. 4, no. 4, pp. 48–56, Dec. 2018.

[5] X. Wang, Z. Wang, M. Gu, D. Xiao, J. He, and A. Emadi, "Diagnosis-free self-healing scheme for open-circuit faults in dual three-phase PMSM drives," *IEEE Trans. Power Electron.*, vol. 35, no. 11, pp. 12053–12071, Nov. 2020.

[6] X. Wang, Z. Wang, Z. Xu, M. Cheng, W. Wang, and Y. Hu, "Comprehensive diagnosis and tolerance strategies for electrical faults and sensor faults in dual three-phase PMSM drives," *IEEE Trans. Power Electron.*, vol. 34, no. 7, pp. 6669–6684, Jul. 2019.

[7] E. Levi, "Multiphase electric machines for variable-speed applications," *IEEE Trans. Ind. Electron.*, vol. 55, no. 5, pp. 1893–1909, May 2008.

[8] Z. Wang, Y. Wang, J. Chen, and Y. Hu, "Decoupled vector space decomposition based space vector modulation for dual three-phase three-level motor drives," *IEEE Trans. Power Electron.*, vol. 33, no. 12, pp. 10683–10697, Dec. 2018.

[9] B. Ge, F. Z. Peng, A. T. de Almeida, and H. Abu-Rub, "An effective control technique for medium-voltage high-power induction motor fed by cascaded neutral-point-clamped inverter," *IEEE Trans. Ind. Electron.*, vol. 57, no. 8, pp. 2659–2668, Aug. 2010.

[10] Q. Wei, L. Xing, D. Xu, B. Wu, and N. R. Zargari, "Modulation schemes for medium-voltage PWM current source converter-based drives: An overview," *IEEE J. Emerg. Sel. Topics Power Electron.*, vol. 7, no. 2, pp. 1152–1161, Jun. 2019.

[11] J. Holtz and N. Oikonomou, "Fast dynamic control of medium voltage drives operating at very low switching frequency—An overview," *IEEE Trans. Ind. Electron.*, vol. 55, no. 3, pp. 1005–1013, Mar. 2008.

[12] A. Edpuganti and A. K. Rathore, "A survey of low switching frequency modulation techniques for medium-voltage multilevel converters," *IEEE Trans. Ind. Appl.*, vol. 51, no. 5, pp. 4212–4228, Sep./Oct. 2015.

[13] P. Karamanakos and T. Geyer, "Guidelines for the design of finite control set predictive controllers," *IEEE Trans. Power Electron.*, vol. 35, no. 7, pp. 7434–7450, Jul. 2020.

[14] J. Rodríguez *et al.*, "State of the art of finite control set model predictive control in power electronics," *IEEE Trans. Ind. Inform.*, vol. 9, no. 2, pp. 1003–1016, May 2013.

[15] T. Geyer and D. E. Quevedo, "Performance of multistep finite control set model predictive control for power electronics," *IEEE Trans. Power Electron.*, vol. 30, no. 3, pp. 1633–1644, Mar. 2015.

[16] T. Geyer, "Generalized model predictive direct torque control: Long prediction horizons and minimization of switching losses," in *Proc. 48th IEEE Conf. Decis. Control/28th Chin. Control Conf.*, Shanghai, China, 2009, pp. 6799–6804.

[17] T. Geyer, G. Papafotiou, and M. Morari, "Model predictive direct torque control—Part I: Concept, algorithm, and analysis," *IEEE Trans. Ind. Electron.*, vol. 56, no. 6, pp. 1894–1905, Jun. 2009.

[18] Z. Wang, J. Chen, and M. Cheng, "Modeling and control of neutral-point-clamping (NPC) three-level inverters fed dual-three phase PMSM drives," in *Proc. IEEE Energy Convers. Congr. Expo.*, Montreal, QC, Canada, 2015, pp. 6565–6572.

[19] W. Xie *et al.*, "Finite-control-set model predictive torque control with a deadbeat solution for PMSM drives," *IEEE Trans. Ind. Electron.*, vol. 62, no. 9, pp. 5402–5410, Sep. 2015.

[20] Z. Wang, X. Wang, X. Yang, C. Wen, Y. Gong, and Y. Hu, "Mitigation of DC-link current ripple for dual three-phase flux-adjustable hybrid PMAC drives using collaborative switching strategy," *IEEE Trans. Ind. Electron.*, vol. 67, no. 9, pp. 7202–7216, Sep. 2020.

[21] M. Norambuena, J. Rodríguez, Z. Zhang, F. Wang, C. Garcia, and R. Kennel, "A very simple strategy for high-quality performance of AC machines using model predictive control," *IEEE Trans. Power Electron.*, vol. 34, no. 1, pp. 794–800, Jan. 2019.

[22] Y. Zhang, B. Zhang, H. Yang, M. Norambuena, and J. Rodríguez, "Generalized sequential model predictive control of IM drives with field-weakening ability," *IEEE Trans. Power Electron.*, vol. 34, no. 9, pp. 8944–8955, Sep. 2019.

[23] K. Zhang *et al.*, "Tolerant sequential model predictive direct torque control of permanent magnet synchronous machine drives," *IEEE Trans. Transp. Electrific.*, vol. 6, no. 3, pp. 1167–1176, Sep. 2020.

[24] Y. Wang, S. Tobayashi, and R. D. Lorenz, "A low-switching-frequency flux observer and torque model of deadbeat–direct torque and flux control on induction machine drives," *IEEE Trans. Ind. Appl.*, vol. 51, no. 3, pp. 2255–2267, May/Jun. 2015.

[25] J. Rodríguez, J. Pontt, P. Cortes, and R. Vargas, "Predictive control of a three-phase neutral point clamped inverter," in *Proc. IEEE 36th Power Electron. Spec. Conf.*, Recife, Brazil, 2005, pp. 1364–1369.

[26] Y. Zhang, Y. Bai, H. Yang, and B. Zhang, "Low switching frequency model predictive control of three-level inverter-fed IM drives with speed-sensorless and field-weakening operations," *IEEE Trans. Ind. Electron.*, vol. 66, no. 6, pp. 4262–4272, Jun. 2019.

Kailiang Yu (Student Member, IEEE) received the M.S. degree in electrical engineering from the School of Electrical Engineering, Huazhong University of Science and Technology, Wuhan, China, in 2019, and the B.E. degree in electrical engineering, in 2016, from the School of Electrical Engineering, Southeast University, Nanjing, China, where he is currently working toward the Ph.D. degree.

His research interests include the control of multiphase permanent-magnet synchronous motor and parameter estimation.

Xueqing Wang (Member, IEEE) received the B.S. degree from Tianjin University of Science and Technology, Tianjin, China, in 2014, and the M.S. and Ph.D. degrees from Southeast University, Nanjing, China, in 2016 and 2020, respectively, all in electrical engineering.

From 2018 to 2019, he was a Joint Ph.D. Student with the McMaster Automotive Resource Centre, McMaster University, Hamilton, ON, Canada. He is currently an Associate Research Fellow with the College of Electrical Engineering, Sichuan University, Chengdu, China. His research interests include fault diagnosis and tolerant control of motor drive, control of multiphase permanent-magnet synchronous motor, and multilevel pulsewidth modulation strategy.

Minrui Gu (Student Member, IEEE) received the B.S. degree in electrical engineering from Nanjing University of Science and Technology, Nanjing, China, in 2019. He is currently working toward the M.S. degree in electrical engineering with Southeast University, Nanjing, China.

His research interests include multilevel converters, multilevel pulsewidth modulation strategy, and control of multiphase permanent-magnet synchronous motor.

Zheng Wang (Senior Member, IEEE) received the B.Eng. and M.Eng. degrees from Southeast University, Nanjing, China, in 2000 and 2003, respectively, and the Ph.D. degree from The University of Hong Kong, Hong Kong, in 2008.

From 2008 to 2009, he was a Postdoctoral Fellow with Ryerson University, Toronto, ON, Canada. He is currently a Full Professor with the School of Electrical Engineering, Southeast University. His research interests include electric drives, power electronics, and renewable power generation. In these fields, he has authored more than 100 internationally refereed papers, one English book by IEEE-Wiley Press, and two English book chapters.

Dr. Wang was the recipient of the IEEE PES Chapter Outstanding Engineer Award, Outstanding Young Scholar Award of Jiangsu Natural Science Foundation of China, and several paper awards of journals and conferences. He is an Associate Editor for the IEEE TRANSACTIONS ON INDUSTRIAL ELECTRONICS and *Journal of Power Electronics*.

Ming Cheng (Fellow, IEEE) received the B.Sc. and M.Sc. degrees from the Department of Electrical Engineering, Southeast University, Nanjing, China, in 1982 and 1987, respectively, and the Ph.D. degree from the Department of Electrical and Electronic Engineering, University of Hong Kong, Hong Kong, in 2001.

Since 1987, he has been with Southeast University, where he is currently a Distinguished Professor with the School of Electrical Engineering and the Director of the Research Center for Wind Power Generation. From January to April 2011, he was a Visiting Professor with the Wisconsin Electric Machine and Power Electronics Consortium, University of Wisconsin, Madison, WI, USA. His teaching and research interests include electrical machines, motor drives for EV, and renewable energy generation. He has authored or coauthored more than 300 technical papers and four books, and is the holder of 70 patents in these areas.

Dr. Cheng is a fellow of the Institution of Engineering and Technology. He was the Chair and an Organizing Committee Member for many international conferences. He was a Distinguished Lecturer of the IEEE Industry Applications Society from 2015 to 2016.